



CHORUS

This is the accepted manuscript made available via CHORUS. The article has been published as:

Origin of the magnetic field enhancement of the spin signal in metallic nonlocal spin transport devices

A. J. Wright, M. J. Erickson, D. Bromley, P. A. Crowell, C. Leighton, and L. O'Brien

Phys. Rev. B **104**, 014423 — Published 20 July 2021

DOI: [10.1103/PhysRevB.104.014423](https://doi.org/10.1103/PhysRevB.104.014423)

2 **Origin of the magnetic field enhancement of the spin signal in metallic non-local spin**
3 **transport devices**

4 A. J. Wright¹, M. J. Erickson², D. Bromley¹, P. A. Crowell², C. Leighton³ and L. O'Brien^{1,*}

5 ¹ Department of Physics, University of Liverpool, Liverpool, L69 7ZE, UK

6 ² School of Physics and Astronomy, University of Minnesota, MN, 55455, USA

7 ³ Department of Chemical Engineering and Materials Science,

8 University of Minnesota, MN, 55455, USA

9
10 The non-local spin valve (NLSV) enables unambiguous study of spin transport, owing to its
11 ability to isolate pure spin currents. A key principle of NLSV operation is that the ‘spin signal’
12 is invariant under application of in-plane magnetic fields (above the ferromagnetic contact
13 saturation field). Yet, for certain ferromagnet/normal metal pairings in NLSVs, an unexpected
14 field enhancement of the spin signal occurs, presenting a challenge that has, thus far, been
15 difficult to resolve with existing models. By correlating the extracted spin transport parameters
16 with material, temperature and field dependencies, in this work we identify field-quenching of
17 magnetic impurity scattering as the origin of this effect, confirmed by excellent agreement
18 between our results and field-dependent Kondo theory. In addition to addressing this long-
19 standing mystery, our findings highlight a potential systematic underestimation of spin
20 transport parameters. By identifying signature field and temperature dependencies, we provide
21 here a relatively simple means to isolate and quantify this additional relaxation mechanism.

22 *Corresponding author: lobrien@liverpool.ac.uk

I. INTRODUCTION

1
2 The controlled transport and manipulation of spins in metals offers the prospect of various
3 technological advances in sensing, logic, and data storage. As an example, the problematic
4 resistance scaling at low dimensions¹⁻³ of magnetic tunnel junctions in hard disk drive read
5 head sensors provides a clear motivation to develop all-metal-based alternatives. Efforts to
6 further understand the flow of spins between, and relaxation within, ferromagnetic (FM) and
7 non-magnetically-ordered metals (NM)⁴⁻²², thus continue to gather pace. Despite this concerted
8 effort, key fundamental questions remain open. Among these, the impact of specific scattering
9 sources on spin relaxation in NMs is a recurring theme^{11,21,23-25}, as are the origins of several
10 field-dependent magnetoresistive effects.^{6,26-28} Light metals, such as Cu and Al, offer an
11 excellent testing ground to understand such issues. In essence, the low resistivity and spin-orbit
12 coupling (SOC) in such metals result in relatively long spin lifetimes, τ_s , where specific
13 relaxation mechanisms can be intentionally introduced, e.g., through tuning disorder;²⁹ doping
14 with high SOC³⁰ or magnetic impurities;¹³ or manipulation of interfaces³¹ and surfaces.^{8,22,23}

15 The non-local spin valve (NLSV) geometry offers a particularly simple, versatile means to
16 probe spin transport in light metals with long τ_s .⁵ Fig. 1(a) shows a scanning electron
17 microscope (SEM) image of a typical nanoscopic metallic NLSV device. In the NLSV
18 geometry, a NM channel is contacted by two FM nanowires, FM_{inj} and FM_{det} , separated by a
19 distance, d . A charge current, I , flowing from I^+ to I^- (see Fig. 1(a)) becomes spin-polarized
20 in FM_{inj} , thus injecting spins into the NM, which subsequently diffuse along the NM channel
21 in the form of a pure spin current. The resulting spin-accumulation reaching FM_{det} can be
22 detected *via* the potential difference, V_{NL} , that develops between FM_{det} and the NM, i.e.,
23 between V^+ and V^- , which can then be normalized by I to give a non-local transimpedance,
24 $R_{NL} = V_{NL}/I$. Inevitably, in addition to the spin-accumulation signal, the measured R_{NL} also
25 contains contributions from spurious effects, including finite current spreading³² and

1 thermoelectric voltages.^{33–36} To mitigate their impact on measurements, the standard approach
 2 is to toggle the magnetization of the FM contacts, from parallel (P) to anti-parallel (AP), with
 3 the difference between the two states, $\Delta R_{NL} = R_{NL}^P - R_{NL}^{AP}$, theoretically isolating only the ‘spin
 4 signal’. Equivalently, one can explicitly calculate the background contribution from the
 5 average of the two states, as $R_b = (R_{NL}^P + R_{NL}^{AP})/2$. The spin signal is then given by $R_{spin} =$
 6 $R_{NL}^P - R_b$, as is the approach taken here. We note that these two approaches are mathematically
 7 equivalent, save for a factor of 2, i.e., $\Delta R_{NL} = 2R_{spin}$.

8 An example of the in-plane magnetic field, $H||y$, dependence of $R_{NL}(H)$ is shown in Fig.
 9 1(b) for a Cu/Fe NLSV with $d = 750$ nm, over a moderate H range (up to 100 mT) and at a
 10 measurement temperature, $T = 5$ K. Both forward and reverse sweeps are shown, and R_{NL}^P ,
 11 R_{NL}^{AP} and R_b are clearly visible as the two FMs switch relative orientation. By measuring R_{spin}
 12 in devices with varying d , and fitting $R_{spin}(d, T)$ using a suitable model,^{15,37} key spin transport
 13 parameters may be extracted for the NM channel under investigation, particularly the
 14 characteristic NM spin diffusion length, λ_N , and so τ_s , *via* the usual diffusion relation ($\lambda_N =$
 15 $\sqrt{D\tau_s}$, where D is the electron diffusivity).

16 These underlying principles of operation have been essential in establishing a consistent
 17 picture of spin relaxation in NLSVs. Efforts have now largely confirmed that in nanoscopic
 18 NLSVs based on low SOC metals, relaxation is dominated by the Elliot-Yafet (EY)
 19 mechanism:^{38,39} for a scattering source i (e.g., phonons, grain boundaries, impurities, *etc.*),
 20 $1/\tau_{s,i} = 1/\beta_i\tau_{e,i}$, where $\tau_{e,i}$ represents the momentum relaxation time due to defect type i ,
 21 and β_i is the corresponding EY parameter.⁴⁰ Empirically, these rates can be summed using
 22 what is essentially Matthiessen’s rule for spin transport, to give the total rate:

$$23 \quad \frac{1}{\tau_s} = \sum_i \frac{1}{\beta_i\tau_{e,i}}. \quad (1)$$

1 While a general consensus has emerged supporting this relationship, deconvoluting
2 contributions from specific mechanisms, i.e., determining each β_i , has been a considerable
3 challenge, with, for example, an order of magnitude variation in measurements of the phonon
4 contribution ($\beta_{ph} = 500 - 3570$) extracted from Cu NLSVs.^{13-15,41}

5 A primary source of difficulty in this regard is the surprising non-monotonicity of $R_{spin}(T)$
6 [or equivalently $\Delta R_{NL}(T)$] at low T , particularly in Cu-based NLSVs.^{7,8,10,19,21,36} In such
7 devices the extracted $1/\tau_s$ is found to unexpectedly *increase* at low T , despite $1/\tau_e$ remaining
8 essentially constant, i.e., a striking departure from naïve application of the EY model. Recent
9 works, by ourselves and others, have shown clear evidence that this is a manifestation of the
10 Kondo effect, originating from the presence of magnetic impurities (MIs) in the NM
11 channel,^{6,13,41-46} even at very low (< 100 ppm) concentrations. Additionally, we have shown
12 that the measured spin polarization, α , is suppressed from its intrinsic value by MIs near the
13 FM/NM interface.⁴⁴ Systematic investigation has shown that the increase in $1/\tau_s$ and
14 suppression of α follow the expected MI concentration scaling^{13,42,47-49} and logarithmic T
15 dependence of the Kondo effect, with a characteristic temperature in good agreement with the
16 known Kondo temperature (T_K) of the Cu/FM pairing.⁴⁶ More recently, we have also shown
17 that Kondo spin relaxation can, surprisingly, be subsumed into an EY form, with an extremely
18 low effective $\beta_K = 3/2$,^{43,44} making MI spin relaxation highly efficient. [*cf.* phonon $\beta_{ph} =$
19 (740 ± 200) and grain boundary $\beta_{GB} = (240 \pm 50)$ in MI-minimized NLSVs⁴¹].

20 Interestingly in the context of the above, there is surprisingly clear evidence that a (high)
21 field enhancement of R_{NL} exists in certain (e.g., Ag/NiFe^{6,26} and Cu/Fe⁴⁶) metallic NLSVs at
22 low T . These indications of a non-constant $R_{spin}(H)$ are significant as they risk undermining
23 much of the previously established knowledge of spin transport in NLSVs. Specifically, a key
24 tenet of NLSV operation is that R_{spin} (or ΔR_{NL}) reliably measures *only* the spin signal and is,

1 for example, field-independent (when the magnetizations of the contacts are parallel to the
 2 field). Understanding the origin of this field enhancement is the main focus of this work. As an
 3 example, Fig. 1(c) shows $R_{NL}(H)$, taken under identical conditions to that of Fig. 1(b), but now
 4 over a larger applied field range of ± 9 T. The field steps used here (~ 100 mT) are larger than
 5 the FM coercivities (< 60 mT), so the low H switching seen in Fig. 1(b) is no longer visible.
 6 The low coercivity ensures that both contacts are parallel over the entire measurement span, so
 7 we designate this curve $R_{NL}^P(H)$. R_{NL}^P is clearly not constant, however, with a monotonic
 8 increase found on increasing $|H|$. R_{spin} is indicated schematically in Fig. 1(c), from which it
 9 is apparent that the field enhancement is *substantial* compared to the original low-field spin
 10 signal, in many cases exceeding R_{spin} in Cu/Fe devices. We define this field enhancement,
 11 $\delta R_{NL}(H)$ as the difference between R_{NL}^P at zero field and at a given field H :

$$12 \quad \delta R_{NL}(H) = R_{NL}^P(H) - R_{NL}^P(0). \quad (2)$$

13 A rigorous explanation of this low T effect has remained largely elusive. Multiple works have
 14 investigated qualitatively similar observations, but none can consistently explain all trends. The
 15 most directly comparable studies,^{6,26} using all-metal Ag/NiFe NLSVs, ascribe the field
 16 dependence to screening of scattering from paramagnetic MIs or magnetic clusters, due to
 17 alignment with an applied field. Correlating this picture with the T and H dependence of
 18 $R_{NL}(H)$ has been problematic, however, with a lack of ideal agreement between data and
 19 models based on $S = 1/2$, Brillouin-like scaling with temperature and field.

20 In this work we perform an extended investigation into the field-dependence of R_{NL} in
 21 metallic NLSVs. By varying the FM (Fe, Co, Ni₈₀Fe₂₀) and NM (Cu, Al) pairings, we
 22 demonstrate that the magnitude of $\delta R_{NL}(H)$ is clearly linked to the ability of the NM to host
 23 MIs. In Al, where local magnetic moments are not supported on 3d transition metal
 24 impurities,⁴⁷⁻⁴⁹ no high-field dependence of R_{NL} is found. In Cu, where the effect is strong,

1 measurements of δR_{NL} as a function of d , T and H reveal an isotropic field dependence with a
2 complex T and d relationship. However, taking the critical step of linking δR_{NL} to
3 enhancement of R_{spin} allows us to extract values for $\lambda_N(H, T)$ and $\tau_s(H, T)$ using standard
4 spin diffusion theory. Extending spin transport models to incorporate Kondo
5 magnetoresistance theory, we then demonstrate excellent quantitative agreement between the
6 experimental $1/\tau_s(H, T)$ and Kondo spin relaxation theory. A physical picture thus prevails
7 where the application of H suppresses MI scattering, restoring the expected T dependence and
8 magnitude of the non-local spin signal. As well as solving the long-standing mystery as to the
9 origin of this low- T field enhancement effect, this high field signature therefore acts as a
10 convenient method to distinguish spin relaxation due to MIs in metals. We also note that failure
11 to account for this effect can potentially significantly impact spin transport measurements and
12 conclusions, particularly in Hanle spin precession experiments, and should thus be
13 incorporated into future analyses.

14

15

II. SAMPLE FABRICATION AND EXPERIMENTAL DETAILS

16 NLSV devices were fabricated using multi-angle electron beam evaporation through a
17 suspended shadow mask. The masks consisted of a polymethylglutarimide (PMGI)/
18 polymethyl methacrylate (PMMA) bilayer resist stack and were written using a Vistec
19 EPBPG5000+ electron beam lithography tool, on Si/Si-N (2000 Å) substrates. FM materials
20 were deposited at an angle of 49° normal to the plane of the device at a rate of 0.5 \AA/s . NM
21 materials were deposited normal to the plane of the device at a rate of 1.0 \AA/s . Nominal purities
22 of the FM and NM materials were 99.95% and 99.999% respectively. All materials were
23 deposited in the same vacuum system, with a base pressure of the order of $\sim 10^{-10}$ Torr.
24 Deposition pressures were in the range 8×10^{-10} to 4×10^{-8} Torr. Thicknesses were calibrated

1 using grazing incidence x-ray reflectivity and monitored during growth using quartz crystal
 2 monitors. A nucleation pad on one of the FM contacts in each device was used to assist domain
 3 wall nucleation, reducing the coercivity of that contact, making the antiparallel state more
 4 readily achievable. NM and FM thicknesses were 200 nm and 16 nm, respectively, for all
 5 devices, and widths (~ 200 nm and $\sim 100 - 150$ nm respectively) were obtained directly from
 6 SEM measurements. All devices were annealed at 80°C during processing.⁴²

7 Local resistivity measurements were first used to obtain the FM and NM resistivities, ρ_{FM}
 8 and ρ_N , and verify the transparent interface limit at the FM/NM interface. Momentum
 9 scattering rates due to defects $1/\tau_{e,def}$ and phonons $1/\tau_{e,ph}$ were calculated from these
 10 resistivity measurements using $\rho_N^{-1} = \frac{1}{3} e^2 N(\epsilon_F) v_F^2 \tau_e$, where e is the electron charge, $N(\epsilon_F)$
 11 the Cu density of states at the Fermi energy, and v_F the Fermi velocity, with ρ_{def} estimated
 12 from the 5 K data. Transport measurements were taken using a 13 Hz AC supply at bias currents
 13 from 100 μA to 1 mA. A 3 $\mu\Omega$ noise floor was present in the R_{NL} measurements. At high
 14 temperatures (> 200 K) and large d (> 1500 nm), the R_{NL} signal was dominated by this noise
 15 floor. An 8% uncertainty in device dimensions was also present.

16

17

III. RESULTS

18

A. Material dependence of δR_{NL}

19 To-date, only limited combinations of FM and NM materials (Cu/Fe⁴⁶ and Ag/NiFe^{6,26}) have
 20 been tested in all-metal NLSVs at relatively high fields. Here, we expand this parameter space
 21 through NLSVs fabricated using Fe, Co and Ni₈₀Fe₂₀ as the FM, and Cu or Al as the NM. The
 22 field dependence of δR_{NL} for different material combinations is shown in Fig. 2 and represents
 23 a key result of our work. Data are shown here for devices with $d = 250$ nm, at $T = 5$ K and,
 24 for direct comparison, they are normalized by R_{spin} in order to compensate for differences in,

1 e.g., FM current polarization, α , and FM (NM) resistivity, ρ_{FM} (ρ_N), etc. We first highlight the
2 Cu/Fe case (red squares). These are the equivalent data to those in Fig. 1(c), once again showing
3 a monotonic increase in $\delta R_{NL}/R_{spin}$ up to the largest fields accessible ($\mu_0 H = 9$ T). Inspection
4 across all other samples shows an approximately similar curve shape to these Cu/Fe data, with
5 δR_{NL} monotonically rising, well beyond the saturation magnetization, M_s , of the respective
6 FMs ($M_s < 2$ T in all cases, ruling out FM contact rotation as a contributing factor). Comparing
7 devices, however, clear differences in the normalized magnitude of δR_{NL} are evident. Looking
8 first at the Cu/Co, Cu/Fe and Cu/Ni₈₀Fe₂₀ devices, it is clear that a large variation in
9 $\delta R_{NL}/R_{spin}$ occurs across the choice of FM materials. Equally, considering Cu/Fe and Al/Fe,
10 a noticeable dependence on the choice of NM material is found: whereas a large $\delta R_{NL}/R_{spin}$
11 is seen in Cu/Fe devices, almost no field dependence is observed for Al/Fe. The $\delta R_{NL}/R_{spin}$
12 behavior is thus dependent on *both* the FM *and* NM material choices.

13 Similar field-dependent trends are also found in other spintronic devices, including three
14 terminal spin valve measurements of semiconductors,⁵⁰ hydrogenated graphene NLSVs,⁵¹ and
15 heavy metal magnetoresistance measurements,⁵² attributed to precession from inhomogeneous
16 magnetostatic fields, local moment exchange interactions, or Hanle precessional
17 magnetoresistance, respectively. In the case of light metal NLSVs, the non-local measurement
18 (limiting the impact of contact relaxation), metallic nature of the transport, extended field
19 dependence (>9 T), and low SOC (and spin Hall angle) rules out each of these explanations.

20 Instead, as with earlier work on MI effects in spin transport, we return to the stark correlation
21 between the ability of the host NM to support MIs arising from the FM, and (in this case) the
22 magnitude of $\delta R_{NL}(H)$. Specifically, Cu readily hosts local magnetic moments on dissolved
23 3d transition metal impurities, whereas Al (primarily due to its high Fermi level) does not,^{47–49}
24 a trend that is precisely reflected in the magnitudes observed in Fig. 2. This is further supported

1 by $\delta R_{NL}/R_{spin}$ in Al interlayer (Al-IL) devices, where a thin ($\sim 5\text{nm}$) layer is deposited between
 2 the Cu and Fe layers. Due primarily to the low diffusivity of Fe in Al, the Al-IL greatly reduces
 3 the concentration of Fe impurities in the channel. As a consequence, Cu/Al-IL/Fe devices
 4 exhibit a weak (but non-zero) high field dependence.

5 **B. Determining the origin of δR_{NL}**

6 A natural implication of this correlation between local moment formation and the high field
 7 dependence is that δR_{NL} arises from a spin transport effect, related to MI-driven spin
 8 relaxation. Before continuing with a MI-based analysis, including detailed comparison between
 9 datasets, we first consider other potential phenomena, unrelated to spin transport, as the
 10 potential origins of $\delta R_{NL}(H)$, e.g., field-dependent thermoelectric^{33,34,53} or current spreading³²
 11 effects. In such cases, δR_{NL} would be expected to correlate broadly with the field-independent
 12 background $R_b = (R_{NL}^P + R_{NL}^{AP})/2$, in sign, magnitude, d or T dependence.

13 To test this, in Fig. 3(a) and (b), we show the temperature evolution of δR_{NL} and R_b for
 14 Cu/Fe NLSVs of varying d , and provide a direct comparison of the two in Fig. 3 (d). Examining
 15 Fig. 3(a) and (b), we note that the magnitude of δR_{NL} is relatively large, at times exceeding
 16 that of R_b and R_{spin} [shown in Fig. 3(c)]. Field-dependent corrections to R_b from current
 17 spreading, of order $\omega_c \tau_e$ (where ω_c is the cyclotron frequency)³², are weak in comparison [at
 18 most of the order 10^{-2} at 9 T for our longest measured $\tau_e \approx 50$ fs ($T = 5$ K)]³², ruling out current
 19 spreading as the origin of δR_{NL} . Further examining Fig. 3(a) and (b), it is also clear that there
 20 is no correlation between the evolution of δR_{NL} and R_b : Whereas δR_{NL} decreases with both
 21 increasing T and d (Fig. 3(a)), R_b appears largely independent of these parameters in Cu/Fe
 22 (Fig. 3(b)). Comparing different materials pairings (as shown in Supplemental Material Fig.
 23 S1⁵⁴) yields further inconsistencies in the signs and magnitudes of δR_{NL} and R_b , which are
 24 incompatible with the possibility that δR_{NL} arises from current-spreading or thermoelectric

1 effects. Thus, we can convincingly rule out contributions from conventional (non-spin)
2 transport phenomena, which otherwise determine R_{β} .

3 We next consider magnetothermoelectric (e.g., a field-dependent spin-Seebeck
4 contribution), or weak (anti)localization effects, which are anisotropic with respect to the
5 applied field direction.²⁷ Comparing $R_{NL}(H)$ for different field directions, as in Fig. 3(f),
6 $\delta R_{NL}(H)$ is found to be isotropic with respect to the direction of the applied field. Here, we
7 compare $R_{NL}(H)$ for in-plane (H_y) and out-of-plane (H_z) magnetic fields at $T = 5$ K (other
8 temperatures are shown in Supplemental Material Fig. S2⁵⁴). Out-of-plane measurements are
9 shown for initial parallel and anti-parallel alignment of the FM contacts, and are essentially
10 Hanle effect measurements: the oscillations in R_{NL} thus arise from Larmor precession of
11 conduction electron spins about H_z , decaying as the magnetizations of FM_{inj} and FM_{det} rotate
12 to align with the field. These in-plane and out-of-plane measurements were taken at different
13 times, and inevitably there is a small difference in the zero-field offset to R_{NL} . For ease of
14 comparison, the offset in the in-plane measurements has been shifted (by $\sim 30 \mu\Omega$), to match
15 that of the parallel, out-of-plane measurement at zero field. Beyond the saturation field of the
16 FM contacts (1.8 T), the out-of-plane R_{NL} for both parallel and anti-parallel orientations
17 increase exactly as the in-plane R_{NL} does. This is to say that $\delta R_{NL}(H)$ is independent of the
18 direction of applied field, and therefore does not originate from magnetothermoelectric, weak
19 (anti)localization effects, nor current spreading, which would all have an anisotropic
20 dependence on field direction.^{27,28}

21 In contrast, for a given NM/FM pairing, we find that $\delta R_{NL}(\mu_0 H = 9 \text{ T})$ broadly scales with
22 the magnitude of R_{spin} (see Figs. 3(a), (c) and (e) for Cu/Fe, and Supplemental Material Fig.
23 S1⁵⁴ for Cu/Co, Cu/Ni₈₀Fe₂₀ and Al/Fe). While the specific dependence of $\delta R_{NL}(T, d)$ is
24 complex, and $\delta R_{NL}/R_{spin}$ varies between pairings, for a given FM and NM, $\delta R_{NL}(H)$

1 decreases on reduction of R_{spin} , either through increasing T or d (Fig. 3(e)). From this we
2 conclude that $\delta R_{NL}(H)$ has a similar dependence on the spin-dependent parameters of each
3 material, and indeed arises from a pure spin transport effect.

4 We next examine the T dependence of $\delta R_{NL}(H)$. Cu/Fe offers one of the largest field
5 enhancements, and so we focus on this pairing. (Cu/Fe also provides a convenient pairing for
6 testing Kondo-related contributions, due to its relatively high miscibility and an easily
7 accessible $T_K = 30$ K⁴⁷). Fig. 4 displays $\delta R_{NL}(H)$ for a Cu/Fe device with $d = 250$ nm, across
8 a T range of 5-250 K. As well as increasing with field, δR_{NL} clearly decreases with increasing
9 T . Qualitatively, such scaling is commensurate with the saturation of paramagnetic MI
10 moments under increasing field or decreasing temperature. However, plotting the normalized
11 δR_{NL} vs. $\mu_B \mu_0 H / k_B T$ (inset) fails to collapse the data onto a single functional form, as might
12 be anticipated for the response of free moments under field. Furthermore, δR_{NL} shows a
13 $\mu_B \mu_0 H / k_B T$ dependence that is not only far stronger than expected for $S = 1/2$ MIs, (for all
14 but the lowest 5 K data) but is also poorly described by a classical Langevin expression, where
15 the fitted J varies dramatically with T (see Supplemental Material Fig. S3⁵⁵). A similar
16 observation was made in references 6 and 26, and was attributed to the finite magnetic shape
17 anisotropy energy of clustered MIs. In our devices similar $\delta R_{NL}(H)$ is observed across
18 different material pairings, therefore analysis based on magnetic shape anisotropy would
19 require similar clustering of MIs across these pairings. However, the range of thermodynamic
20 solubilities are unlikely to produce identical distributions and precipitations of (potentially
21 clustered) MIs, seeming to disfavour such a model, and suggesting a fundamentally different
22 mechanism is at play.

23

24

C. Extracting spin transport characteristics

Acknowledging that δR_{NL} arises from a spin transport effect, we must accept that any changes in $\delta R_{NL}(T)$ are manifestly convolved with the T -dependent variation of the key relevant NLSV material parameters, particularly $\tau_s(T)$, $\alpha(T)$, $\rho_N(T)$ and $\rho_{FM}(T)$. Given that all other key parameters are either constant (d , and the NM thickness, t_N) or have a weak H dependence (ρ_N , ρ_{FM} , λ_F), we proceed by considering the (MI) scattering contribution to τ_s and α , which are now anticipated to depend on H , as well as T . To extract these terms, a comprehensive study of $R_{NL}(H)$ in Cu/Fe NLSVs was performed at various d (250-2000 nm) and T (5-250 K).

Reasoning that the field dependence of R_{NL} can be subsumed into τ_s and α is equivalent to defining a field-dependent NLSV spin signal, $R_{spin}(H) = R_{spin}(0) + \delta R_{NL}(H)$, where $R_{spin}(0) = R_{NL}^P(0) - R_b$ as defined earlier. This model is based on the assumption that R_b is independent of the magnetic field, which is easily verified following our discussion in Sec. III. B. To calculate $R_{spin}(H)$, we obtained $\delta R_{NL}(H)$ data for a range of T and d values, via equation 2. Because it is convenient to be able to represent the data as a continuous function of H , we adopt for now a purely empirical fitting function:

$$\delta R_{NL}(H) = \left| A_1 \left(\coth x - \frac{1}{x} \right) \right| - A_2 |\mu_0 H| \quad (3)$$

where $x = \mu_0(H - H_0)/b$, and A_1 , A_2 , b and H_0 are constant fitting parameters. We emphasize that our use of equation (3) is solely as a representation of the data, and offers little physical insight. The fitted curves (shown by the solid lines in Fig. 4) are combined with measurements of $R_{spin}(0)$ to obtain $R_{spin}(H)$ for any given field within ± 9 T, and at selected $d = 250$ -2000 nm and $T = 5$ -250 K. Representative values of $R_{spin}(d, H)$ are shown in Fig. 5(a) for $\mu_0 H = 0, 1, 3, 5$ and 9 T, at $T = 5$ K. Despite the varying magnitude of δR_{NL} vs. H, T

1 and d , $R_{spin}(d, H)$ assumes the expected functional form for all H : a simple exponential decay
 2 at high d with the deviation at low d that is a hallmark of NLSV spin diffusion in the low
 3 interface resistance limit. Encouraged by this d dependence, we fit these data using a standard
 4 1-D magnetoelectronic circuit theory solution for $R_{spin}(H)$, applied to the NLSV geometry in
 5 the transparent interface limit:⁵⁶

$$6 \quad R_{spin}(H) = 2 \frac{\alpha_{eff}^2 R_F^2}{(1 - \alpha_{eff}^2)^2 R_N} \frac{\exp\left(-\frac{d}{\lambda_N}\right)}{\left[1 + \frac{2R_F}{(1 - \alpha_{eff}^2)R_N}\right]^2 - \exp\left(-\frac{2d}{\lambda_N}\right)}. \quad (4)$$

7 Here, $R_N = \rho_N \lambda_N / w_N t_N$ and $R_F = \rho_F \lambda_F / w_F w_N$ are the NM and FM spin-resistances, with
 8 ρ_N (ρ_F) and w_N (w_F) the respective resistivities and widths; and t_N the NM thickness. In
 9 equation (4) we employ an effective spin polarization, α_{eff} , to account for the presence of MI-
 10 induced depolarization at the NM/FM interfaces⁴² and to distinguish it from the intrinsic FM
 11 polarization, α . To constrain the fitting, we experimentally measure ρ_N on the same NLSVs,
 12 and ρ_F on nanowires of identical cross-sectional dimensions. All dimensions were measured
 13 using SEM for each device, and λ_F was constrained to a value of 4 nm through empirical
 14 scaling with ρ_F .^{46,57} Only λ_N and α_{eff} thus remain as fitting parameters, and these two are
 15 readily separable through the high- d exponential dependence, which is determined only by λ_N .
 16 Extracted values of $\lambda_N(T)$ for selected field values are shown in Fig. 5(b), along with the
 17 corresponding $1/\tau_s(T)$ (through the diffusion relation, $\lambda_N = \sqrt{D\tau_s}$) in Fig. 5(c). In Fig. 5(d)
 18 the relevant $\alpha_{eff}(T)$ are displayed.

19 **D. Temperature and field dependence of spin transport**

20 Looking first at the zero-field $\lambda_N(T)$ data in Fig. 5(b), an initial increase in λ_N with decreasing
 21 T is observed from 250 K to 40 K, as phonon scattering is progressively frozen out. Below 40
 22 K a noticeable downturn is then observed, producing a peak in $\lambda_N(T)$. This peak, widely seen

1 in other works^{7,8,11,21}, and clearly contrasting with the naïvely expected (monotonic) EY-like
 2 behaviour,^{40,58} is qualitatively similar to that seen in low-purity Cu/Fe NLSVs.^{41,42,46} There, it
 3 is attributed to Kondo relaxation arising from dilute MIs, present throughout the channel (even
 4 in initially high-purity NM materials, NM/FM interdiffusion will inevitably introduce MIs into
 5 the channel if the solubility is high enough). We note that, at low T , λ_N should approach a
 6 constant value due to the unitary limit of Kondo relaxation. As shown in our previous work,
 7 this is readily observed in our devices when $T \ll 30$ K,⁴⁶ and is particularly prevalent in devices
 8 with high MI concentrations and/or higher Kondo temperatures^{42,45}. Indeed this effect is also
 9 evident here, although the coarser T steps limit quantitative comparison.

10 Although on first inspection the downturn in $\lambda_N(T)$ is a seemingly weak effect, we emphasize
 11 that the full impact of MI relaxation can only be assessed from the departure from conventional
 12 spin relaxation due to phonon and T -independent defect scattering alone. To demonstrate this,
 13 we estimate the expected $1/\tau_s(T)$ and $\lambda_N(T)$ for EY-type scaling, using equation (1) for
 14 phonon and defect scattering. $1/\tau_{e,def}$ and $1/\tau_{e,ph}$ are calculated as described in Sec. II, and
 15 we use typical values for phonon and defect EY parameters, $\beta_{ph} = 740$ and $\beta_{def} = 240$,
 16 respectively, previously determined from devices in which MI effects were minimized.⁴¹
 17 (Under such conditions, grain boundaries were found to dominate defect scattering, and so we
 18 use $\beta_{def} = \beta_{GB}$.) λ_N values were then calculated from $1/\tau_s$ using the diffusion relation $\lambda =$
 19 $\sqrt{\tau D}$, where D is the diffusivity taken from local resistivity measurements. The corresponding
 20 curve, represented by the black dashed line in Fig. 5(b), demonstrates the stark impact of MI
 21 spin relaxation, which results in $\sim 30\%$ suppression of λ_N at 5 K. In this context, the impact of
 22 applying H becomes clearer. Specifically, examining $\lambda_N(T)$ with increasing H we find a simple
 23 trend where $\lambda_N(T)$ steadily rises until it approaches the very same monotonic dependence
 24 expected in Kondo-minimized devices. We conclude, therefore, that the field acts to quench T -
 25 dependent MI (i.e., Kondo) scattering.

1 Equivalent behavior is observed in $1/\tau_s$, as shown in Fig. 5(c), where the $H = 0$ scattering
 2 rate initially decreases with T , down to 90 K, before unexpectedly increasing on further
 3 cooling. Both the magnitude and T dependence of this behaviour are in good agreement with
 4 the $1/\tau_s$ seen in other Cu/Fe devices^{41,42,46}, but once again strongly contrasts with expected EY
 5 theory (black dashed curve). At this point we note that in the Kondo model, T_K determines a
 6 characteristic temperature scale about which the scattering rate becomes enhanced, rather than
 7 any critical temperature. The increase in $1/\tau_s$ about $T \sim 25$ K is therefore consistent with the
 8 onset of the Kondo effect in Cu/Fe ($T_K = 30$ K).^{46,47,59} While this upturn in $1/\tau_s$ at low T has
 9 now been widely observed, the restoration of $1/\tau_s$ under increasing H is new here and is stark.
 10 Under application of the field, $1/\tau_s$ approaches the expected EY dependence, which is nearly
 11 restored by $\mu_0 H = 9$ T. Despite the action of H in quenching Kondo scattering, a noticeable
 12 shoulder remains at low T , even at $\mu_0 H = 9$ T. As we will detail below, this shoulder is a
 13 hallmark of such MI scattering, and is produced by the competition between different energy
 14 scales in the system, notably the Kondo singlet, thermal and Zeeman energies.

15 We next consider these observations further by comparing Cu/Fe with other NM/FM
 16 combinations. While we do not make in-depth quantitative comparison, we do examine the
 17 (normalized) residual scattering rate, $1/\tau_{s,res} = 1/\tau_s^{zero\ field} - 1/\tau_s^{high\ field}$, for Cu/Co,
 18 Cu/NiFe and Cu/Fe, where “high field” refers to the highest field available (4.5 T for Cu/Co, 9
 19 T otherwise).⁵⁴ From the preceding discussion, in essence, $1/\tau_s^{high\ field}$ corresponds to the
 20 relaxation rate under the near-complete quenching of MI scattering, but without any changes
 21 to $1/\tau_{s,ph}$. Defined in this way, $1/\tau_{s,res}(T)$ can therefore provide an estimate of the T -
 22 dependence of MI scattering, although it cannot give insight into its overall magnitude.
 23 Additionally, the absolute value of $1/\tau_{s,res}$ is dependent on the material properties of the

1 FM/NM pairings, and so, for suitable comparison between pairings, we normalize the data to
 2 their maximum value.

3 The normalized $1/\tau_{s,res}(T)$ data are shown in Fig. 6, on a logarithmic temperature scale. In
 4 all cases, as expected, $1/\tau_{s,res}$ decreases with temperature. Significantly, Cu/Fe shows a clear
 5 logarithmic T dependence about a temperature range consistent with $T_K = 30$ K. As this data
 6 set is quite complete, we fit the data using the phenomenological Goldhaber-Gordon expression
 7 for Kondo scattering⁶⁰:

$$8 \quad \frac{1}{\tau_{s,res}} = G_0 \left[\frac{T_K'^2}{T^2 + T_K'^2} \right]^s \quad (5)$$

9 where $T_K' = T_K/\sqrt{2^{1/s} - 1}$ and $s = 0.22$ for spin-1/2 MIs^{46,60}. Since the data are normalized,
 10 we fix $G_0 = 1$ and T_K remains as the only free parameter. The fit (solid line) models the data
 11 reasonably well, returning $T_K = (20 \pm 8)$ K, in decent agreement with the expected $T_K = 30$ K.
 12 Encouragingly, this Cu/Fe behavior is reproduced in Cu/Ni₈₀Fe₂₀ (Ni is not expected to show
 13 any Kondo contribution due to the prohibitively high $T_K \sim 1000$ K, thus only Fe moments
 14 should contribute for Cu/Ni₈₀Fe₂₀). In contrast, Cu/Co has a response which is clearly shifted
 15 to higher T , appearing to reach the unitary limit at $T \sim 50$ K. This correlates well with the
 16 increased T_K value for this pairing (Cu/Co has a T_K of either 23 or 500 K depending on whether
 17 the MIs are surface or bulk, respectively^{46,61}), further cementing the relationship between
 18 $\delta R_{NL}(H)$, through $1/\tau_s$, and MI scattering.

19 **E. Fitting the spin relaxation rate, $1/\tau_s$**

20 Given the success of Kondo scattering in qualitatively describing $1/\tau_s(T)$ for Cu/FM NLSVs,
 21 we continue this approach, now quantitatively accounting for the impact of H on $\tau_{s,K}$. Previous
 22 studies of the magnetoresistance of Cu_{1-x}Fe_x and similar alloys have shown that application of
 23 a magnetic field indeed suppresses Kondo scattering at low temperatures,^{62,63} and several

1 qualitatively similar models have been proposed^{64–66}. Here, we use the model derived by
 2 Litvinov,⁶⁴ which most accurately represents Fe impurities in a metallic host. (We have also
 3 performed analysis using the Abrikosov model⁶⁵, which we present in the Supplemental
 4 Material Fig. S4; similar results are produced.⁶⁷) In the Litvinov theory, the Kondo momentum
 5 scattering rate is given by:

$$6 \quad \frac{1}{\tau_{e,K}} = \frac{3\pi c J^2}{32\hbar\varepsilon_F} \times \frac{2 \tanh\left(\frac{Q}{k_B T}\right) - \tanh\left(\frac{Q}{2k_B T}\right)}{\sinh\left(\frac{Q}{k_B T}\right)} \times \left[1 + \frac{3J}{4\varepsilon_F} \ln\left(\frac{k_B T_K^2}{(2k_B T)^2 + Q^2}\right) \right]^{-2} \quad (6)$$

7 where c is the concentration of magnetic impurity atoms, J is the exchange energy between the
 8 magnetic impurity and conduction electrons, and ε_F is the Fermi energy. $Q = \mu_0\mu_B g_i H$ is the
 9 Zeeman energy due to the magnetic field, where g_i is the impurity g -factor (assumed to equal
 10 2). There are two energy scales at play in this equation: the first, which comprises the
 11 hyperbolic terms, describes the magnetization of the magnetic impurities and the competition
 12 between T and H ; the second, which is the modified Kondo term, acts to suppress the scattering
 13 rate, with contributions from the singlet and Zeeman energies.

14 The data in Fig. 5(c) were fit using equations (1) and (6), considering terms from phonon,
 15 T -independent impurities, and Kondo scattering explicitly. Here, $1/\tau_{e,ph}$ and $1/\tau_{e,imp}$ are
 16 known from local measurements of ρ_N , while $J = -0.91$ eV and $\varepsilon_F = 7.0$ eV may be
 17 constrained for Fe;^{44,62} and $\beta_K = 3/2$ is known at zero field.^{44,68} At $H \neq 0$, however, β_K is
 18 expected to vary: the Zeeman energy of the magnetic field breaks the symmetry of spin-flip
 19 Kondo scattering, but not of spin-conserving Kondo scattering, resulting in different field
 20 dependencies and hence a non-constant $\beta_K(H)$ ^{66,69,70}. As discussed further below, the fits
 21 therefore remain underconstrained, with free parameters $\beta_{def}, \beta_{ph}, c$ and $\beta_K(H)$. For
 22 simplicity, we have employed a constant, volume average impurity concentration in the model,
 23 although it is expected that c will vary with distance from the NM/FM interface.⁴² Since

1 $\beta_K(H = 0) = 3/2$, the zero-field data were first fit, returning values of $\beta_{def} = 230$, $\beta_{ph} = 470$,
2 and $c = 890$ ppm. From the earlier discussion, these values are clearly physically reasonable,
3 and fall among those from our prior work, and the work of others.^{9,11,15,18,41} As these parameters
4 are expected to be invariant under H , they were then used as fixed values for the remaining fits,
5 with only $\beta_K(H)$ allowed to vary, significantly constraining the fit. Best fit curves using this
6 approach are shown at select fields by the solid lines in Fig. 5(c), and the variation of the
7 extracted $\beta_K(H)$ is displayed in the inset.

8 It can be clearly seen that this model represents the data well; in particular, the knee observed
9 between $T = 5$ and 50 K at higher fields is accurately reproduced. This is a strong indication
10 that the magnetic field is indeed acting to suppress Kondo scattering in the NM channel, and
11 that the high field dependence of $R_{spin}(H)$ can be quantitatively understood through the
12 quenching of the (T -dependent) singlet scattering. The behavior of β_K is of particular interest.
13 β_K is expected to increase with increasing H , as the alignment of the magnetic impurities
14 freezes out spin-flip Kondo scattering events.⁶⁶ However, as far as we are aware, no prior work
15 has experimentally examined this precise evolution. We thus consider this determination of
16 $\beta_K(H)$ an important dataset for the future understanding of the Kondo effect and its relationship
17 with spin relaxation, and we believe it represents a new challenge to theory to accurately model
18 this observed dependence.

19 **F. Field dependence of the effective current polarization, α_{eff}**

20 Before concluding, as an additional consistency check we consider the behavior of the effective
21 current-polarization, $\alpha_{eff}(H, T)$, as shown in Fig. 5(d). The $\alpha_{eff}(T)$ data for Cu/Al-IL/Fe are
22 also shown here (green diamonds). In the absence of Kondo scattering, α_{eff} should approach a
23 constant on cooling, as in the Al-IL device. In the Cu/Fe device however, this is not the case at
24 small fields: as in the λ_N data, a downturn in α_{eff} is seen at low temperatures, due to Kondo

1 scattering through interdiffused MIs near the NM/FM interface, which is known to suppress
 2 the injected spin polarisation.⁴⁴ Once again, however, the application of a magnetic field
 3 removes this suppression, as clearly shown in Fig. 5(d). By $\mu_0 H = 5$ T, $\alpha_{\text{eff}}(T)$ is in fact
 4 approximately restored to that in the Al-IL device. In reference 44, some of us showed that this
 5 α_{eff} suppression is described by:

$$6 \quad \alpha_{\text{eff}} = \alpha \left\{ 1 - z \left[\frac{1 + \frac{2}{\beta_K} \frac{\tau'_S}{\tau'_e}}{\lambda_N} - \frac{\frac{2}{\beta_K} \frac{\tau'_S}{\tau'_e}}{\lambda_N + \frac{\rho_F}{(1 - \alpha^2) \rho_N} \lambda_F} \right] \frac{\tau'_e}{\tau_{e,K}} \right\} \quad (7)$$

7 where z is the characteristic interdiffusion depth of the magnetic impurities in the NM channel,
 8 which is expected to be of the order of 10's of nm for Cu/Fe,⁴² and τ'_e and τ'_S are the MI-free
 9 momentum and spin relaxation times, respectively. $1/\tau'_e$ and $1/\tau'_S$ were obtained using $1/\tau'_e =$
 10 $1/\tau_e - 1/\tau_{e,K}$ and $1/\tau'_S = 1/\tau_S - 1/\beta_K \tau_{e,K}$, where, $1/\tau_e$ and $1/\tau_S$ are determined from ρ_N
 11 and λ_N , while $1/\tau_{e,K}$ and β_K are the best fit values shown in Fig. 5(c). This leaves z and the
 12 intrinsic spin polarization, α , as the only free parameters in fits. The resulting best fit curves,
 13 shown by the solid lines in Fig. 5(d), reproduce the α_{eff} data well. The extracted values of $\alpha =$
 14 0.4 ± 0.04 and $z = 57 \pm 24$ nm across the data set are also entirely plausible, and comparable to
 15 values obtained in reference 44.

16 It is evident from these results that the field-dependent background effects in R_{NL} can be
 17 understood as the suppression of Kondo scattering in the NM channel. Moreover, by extracting
 18 $1/\tau_S$ and α_{eff} from the $R_{\text{spin}}(d, T)$ data, the suppression of the Kondo scattering can be
 19 effectively modelled by the use of equations (6) and (7). This has clear implications for NLSV
 20 devices based on materials that host MIs and hence have τ_S and α_{eff} reduced by Kondo
 21 scattering. This effect is also likely to be present in more complicated systems, such as those
 22 where MIs have been intentionally introduced, or in complex heterostructures of Kondo active
 23 pairings. Here, relaxation from MIs could dominate and obscure spin lifetime measurements,

1 e.g., through distortion of Hanle spin precession curves, due to the field dependence of both
 2 the saturation background and the spin lifetime. However, we have demonstrated in this work
 3 a simple means to quantify this effect, by application of a magnetic field large enough to
 4 saturate the moments.

5 **G. Exchange field model**

6 Due to the nature of our devices, which contain very low concentrations of dilute MIs, we
 7 discussed $R_{spin}(H)$ above in terms of the physically relevant Kondo scattering regime. For
 8 completeness, however, we may also consider the impact of spin decoherence due to precession
 9 about a random exchange field, arising from MIs, such as those considered by McCreary *et*
 10 *al.*⁵¹ In such an exchange field model, the conduction electrons experience an exchange field
 11 from the impurity moments, with RMS fluctuations, ΔB_{ex} , about the average field $\overline{B_{ex}}$,
 12 occurring on a timescale τ_c , the correlation time. The spin relaxation rate due to this exchange
 13 field is given by:^{51,71}

$$14 \quad \frac{1}{\tau_{ex,s}} = \frac{(\Delta B_{ex})^2}{\tau_c} \frac{1}{(\mu_0 H + \overline{B_{ex}})^2 + \left(\frac{\hbar}{g_e \mu_B \tau_c}\right)^2} \quad (8)$$

15 where \hbar , g_e and μ_B are Planck's constant, the electron g-factor and the Bohr magneton
 16 respectively. Following the procedure in reference 51, we assume $\overline{B_{ex}}$ is described by a
 17 Brillouin function, B_S , through

$$18 \quad \overline{B_{ex}} = \frac{cJS}{g_e \mu_B} B_S(\xi) \quad (9)$$

19 where $\xi \equiv Q/k_B T$, and $B_S(x)$ reduces to $\tanh(x)$ for spin $S = 1/2$ impurities.

20 We reproduce the spin relaxation rate as a function of temperature in Fig. 7(a), and now
 21 attempt to fit it with this exchange field model. ΔB and τ_c are expected to be independent of
 22 the magnetic field, but should vary with T , and we therefore fit $1/\tau_s(H)$ at fixed T using

1 equations (1), (8) and (9), with ΔB and τ_c as free parameters. (This is in contrast to the fitting
2 procedure in Sec. III E, in which we fit $1/\tau_s(T)$ at fixed H .)

3 Although the exchange model appears to fit the data well, the extracted ΔB and τ_c are
4 revealing. These are shown in Fig. 7(b) and (c) respectively, for $c = 100$ ppm and 1000 ppm.
5 We choose 1000 ppm here as this is close to the upper limit of a dilute system, and higher
6 concentrations would be expected to lead to phase separation of Cu and Fe. Concentrations of
7 100 ppm and below are likely more representative of our devices, and we find that, at these
8 concentrations, c has negligible impact on ΔB and τ_c , since $\overline{B_{ex}} \ll \mu_0 H$ in equation (8). Note
9 that the 250 K ΔB and τ_c data have been excluded in Fig. 7(b,c), due to anomalously low and
10 high values, respectively, likely due to the large spread in the $1/\tau_s$ data at this temperature
11 (Fig. 7(a)).

12 Looking first at the $c = 100$ ppm case, $\Delta B(T)$ is seen to fluctuate about a constant value of
13 ~ 1.2 T. Although possible, such a large magnitude of ΔB is unlikely. τ_c also exhibits a strong
14 temperature dependence, increasing with decreasing T , indicative of what would occur at a
15 spin glass transition, for example. It is generally expected that τ_c is constant in both NM and
16 FM materials, changing dramatically only during a phase transition, e.g., spin glass
17 freezing.^{47,72-74} Given the dilute nature of the MIs here, and so the weak inter-MI coupling, we
18 do not believe that this T dependence can be physically realistic, particularly as we are far from
19 the concentrations required for a spin glass transition at this temperature ($c \sim 1\%$ for a
20 transition at around 10 K in $\text{Cu}_{1-x}\text{Fe}_x$).^{75,76}

21 Although unlikely, we nevertheless test the hypothesis of $\tau_c(T)$ indicating a spin glass
22 transition using the conventional description for the critical slowing down of spin dynamics in
23 a spin glass^{47,77}:

$$\tau_C = \tau_0 \left(\frac{T - T_g}{T_g} \right)^{-z\nu} \quad (10)$$

where T_g is the spin glass transition temperature, τ_0 is a characteristic timescale and the exponent $z\nu$ is a constant. We fit the data using equation (10), with τ_0 , T_g and $z\nu$ as free parameters. The resulting fit, shown in Fig. 7(c), models the data reasonably, but fails to completely reproduce the form of $\tau_C(T)$. Moreover, the extracted parameters are $T_g \approx 0$ K and $z\nu = 0.25$. Such a $z\nu$ value is unfeasibly low,⁴⁷ indicating that we are far from a transition at a (finite) T_g near 0 K. It is therefore unlikely that such a spin glass transition is occurring in our devices.

Moving to the behavior of ΔB and τ_C at $c = 1000$ ppm, we find even less physical behavior, with ΔB increasing on cooling to a very large 2.7 T at 5 K, and τ_C varying non-monotonically with T . Such a strong temperature dependence of ΔB , and large magnitude, is clearly unreasonable. Hence, although the exchange model is able to fit the $1/\tau_S$ data, it is not able to provide satisfying physical insight into the T and H variation of $1/\tau_S$ (and thus δR_{NL}), as evidenced by the unreasonable T dependencies of ΔB and τ_C . We therefore conclude that the exchange model is not a suitable description for the field enhancement of R_{NL} we observe in our devices. We do emphasize, however, that this does not rule out such a mechanism becoming active in devices where the NM is (intentionally) more heavily substituted with MIs (thereby introducing MI-MI interactions) or directly exchange-coupled to a FM.³¹ There, it is reasonable to assume such exchange field coupling could be active. Indeed, should the materials in these devices undergo a magnetic phase transition, e.g., FM ordering or spin glass freezing, then it is reasonable to expect this will also contribute to non-monotonicity in $R_{spin}(H, T)$, potentially with comparable magnitudes to the Kondo scattering observed here. These could potentially be identified through the characterization of T_g and $z\nu$.

IV. CONCLUSION

An increase in non-local resistance in NLSVs under the application of an external magnetic field has been previously reported,^{6,26} and is observed here. Through the experimental measurement of a wide range of metallic NM/FM combinations, we demonstrate that the effect is correlated with the ability of the NM metal to host dilute magnetic impurity moments. Considering the field dependence of λ_N and $1/\tau_s$, we have shown that this strong field dependence originates from Kondo scattering in the NM channel, and that application of an external magnetic field quenches this scattering. We have successfully applied a model for Kondo scattering in a magnetic field to describe the spin-flip scattering rate data, demonstrating quantitative agreement with experiment and providing the first measurements of the field dependence of the Kondo EY parameter, $\beta_K(H)$. This work thus resolves the long-standing mystery of the origin of this high field dependence, and points to a systematic underestimation of τ_s in NLSVs where MIs are present. Due to the low value of $\beta_K \sim 3/2$, this effect is significant, and is likely to be measurable in a variety of all-metallic NLSVs. By application of a magnetic field, however, we have demonstrated a simple means to remove the suppression and restore the non-local resistance to its Kondo-free value, obviating the need for additional material considerations or the inclusion of a diffusion-limiting interlayer.

ACKNOWLEDGEMENTS

Work supported by the UK EPSRC, Grant No. EP/P005713/1, and the National Science Foundation under Award Number DMR-1807124. Parts of this work were performed in the Characterization Facility, UMN, which receives partial support from NSF through the MSREC program. Other parts of this work were conducted in the Minnesota Nano Center, which is

- 1 supported by the NSF through the National Nano Coordinated Infrastructure Network, under
- 2 Award Numbers NNCI-1542202 and ECCS-2025124.
- 3

REFERENCES

- ¹ M. Yamada, D. Sato, N. Yoshida, M. Sato, K. Meguro, and S. Ogawa, *IEEE Trans. Magn.* **49**, 713 (2013).
- ² Y.K. Takahashi, S. Kasai, S. Hirayama, S. Mitani, and K. Hono, *Appl. Phys. Lett.* **100**, 052405 (2012).
- ³ M. Takagishi, K. Yamada, H. Iwasaki, H.N. Fuke, and S. Hashimoto, *IEEE Trans. Magn.* **46**, 2086 (2010).
- ⁴ M. Johnson and R.H. Silsbee, *Phys. Rev. Lett.* **55**, 1790 (1985).
- ⁵ F.J. Jedema, A.T. Filip, and B.J. van Wees, *Nature* **410**, 345 (2001).
- ⁶ G. Mihajlović, S.I. Erlingsson, K. Výborný, J.E. Pearson, S.D. Bader, and A. Hoffmann, *Phys. Rev. B* **84**, 132407 (2011).
- ⁷ H. Idzuchi, Y. Fukuma, L. Wang, and Y. Otani, *Appl. Phys. Lett.* **101**, 022415 (2012).
- ⁸ H. Zou and Y. Ji, *Appl. Phys. Lett.* **101**, 082401 (2012).
- ⁹ S. Rakheja, S.C. Chang, and A. Naeemi, *IEEE Trans. Electron Devices* **60**, 3913 (2013).
- ¹⁰ E. Villamor, M. Isasa, L.E. Hueso, and F. Casanova, *Phys. Rev. B* **88**, 184411 (2013).
- ¹¹ E. Villamor, M. Isasa, L.E. Hueso, and F. Casanova, *Phys. Rev. B* **87**, 094417 (2013).
- ¹² S. Chen, H. Zou, C. Qin, and Y. Ji, *Appl. Phys. Express* **7**, 113001 (2014).
- ¹³ J.T. Batley, M.C. Rosamond, M. Ali, E.H. Linfield, G. Burnell, and B.J. Hickey, *Phys. Rev. B* **92**, 220420 (2015).
- ¹⁴ Y. Cai, Y. Luo, C. Zhou, C. Qin, S. Chen, Y. Wu, and Y. Ji, *J. Phys. D: Appl. Phys.* **49**, 185003 (2016).
- ¹⁵ F.J. Jedema, M.S. Nijboer, A.T. Filip, and B.J. van Wees, *Phys. Rev. B* **67**, 085319 (2003).

- ¹⁶ S.O. Valenzuela and M. Tinkham, *Appl. Phys. Lett.* **85**, 5914 (2004).
- ¹⁷ Y. Ji, A. Hoffmann, J.S. Jiang, and S.D. Bader, *Appl. Phys. Lett.* **85**, 6218 (2004).
- ¹⁸ S. Garzon, I. Žutić, and R.A. Webb, *Phys. Rev. Lett.* **94**, 176601 (2005).
- ¹⁹ T. Kimura, T. Sato, and Y. Otani, *Phys. Rev. Lett.* **100**, 066602 (2008).
- ²⁰ X.J. Wang, H. Zou, and Y. Ji, *Phys. Rev. B - Condens. Matter Mater. Phys.* **81**, 1 (2010).
- ²¹ G. Mihajlović, J.E. Pearson, S.D. Bader, and A. Hoffmann, *Phys. Rev. Lett.* **104**, 237202 (2010).
- ²² M. Erekhinsky, A. Sharoni, F. Casanova, and I.K. Schuller, *Appl. Phys. Lett.* **96**, 022513 (2010).
- ²³ N. Poli, M. Urech, V. Korenivski, and D.B. Haviland, *J. Appl. Phys.* **99**, 2004 (2006).
- ²⁴ A. Fert and P.M. Levy, *Phys. Rev. Lett.* **106**, 157208 (2011).
- ²⁵ Y. Otani and T. Kimura, *Philos. Trans. R. Soc. A Math. Phys. Eng. Sci.* **369**, 3136 (2011).
- ²⁶ K. Výborný, G. Mihajlović, A. Hoffmann, and S.I. Erlingsson, *J. Phys. Condens. Matter* **25**, 216007 (2013).
- ²⁷ K.S. Das, F.K. Dejene, B.J. van Wees, and I.J. Vera-Marun, *Phys. Rev. B* **94**, 180403 (2016).
- ²⁸ D. Ruffer, F.D. Czeschka, R. Gross, and S.T.B. Goennenwein, *Appl. Phys. Lett.* **99**, (2011).
- ²⁹ Y. Niimi, D. Wei, H. Idzuchi, T. Wakamura, T. Kato, and Y. Otani, *Phys. Rev. Lett.* **110**, 016805 (2013).
- ³⁰ C. Zhou, F. Kandaz, Y. Cai, C. Qin, M. Jia, Z. Yuan, Y. Wu, and Y. Ji, *Phys. Rev. B* **96**, 094413 (2017).

- ³¹ P.K. Muduli, M. Kimata, Y. Omori, T. Wakamura, S.P. Dash, and Y. Otani, *Phys. Rev. B* **98**, 024416 (2018).
- ³² M. Johnson and R.H. Silsbee, *Phys. Rev. B* **76**, 153107 (2007).
- ³³ F.L. Bakker, A. Slachter, J.P. Adam, and B.J. Van Wees, *Phys. Rev. Lett.* **105**, 1 (2010).
- ³⁴ M. Erekhinsky, F. Casanova, I.K. Schuller, and A. Sharoni, *Appl. Phys. Lett.* **100**, 212401 (2012).
- ³⁵ A. Hojem, D. Wesenberg, and B.L. Zink, *Phys. Rev. B* **94**, 1 (2016).
- ³⁶ F. Casanova, A. Sharoni, M. Erekhinsky, and I.K. Schuller, *Phys. Rev. B* **79**, 1 (2009).
- ³⁷ S. Takahashi and S. Maekawa, *Phys. Rev. B - Condens. Matter Mater. Phys.* **67**, 1 (2003).
- ³⁸ R.J. Elliott, *Phys. Rev.* **96**, 266 (1954).
- ³⁹ Y. Yafet, in *Solid State Phys.* (Academic Press, 1963), pp. 1–98.
- ⁴⁰ P. Monod and F. Beuneu, *Phys. Rev. B* **19**, 911 (1979).
- ⁴¹ J.D. Watts, L. O’Brien, J.S. Jeong, K.A. Mkhoyan, P.A. Crowell, and C. Leighton, *Phys. Rev. Mater.* **3**, 124409 (2019).
- ⁴² L. O’Brien, D. Spivak, J.S. Jeong, K.A. Mkhoyan, P.A. Crowell, and C. Leighton, *Phys. Rev. B* **93**, 014413 (2016).
- ⁴³ J.D. Watts, J.S. Jeong, L. O’Brien, K.A. Mkhoyan, P.A. Crowell, and C. Leighton, *Appl. Phys. Lett.* **110**, 222407 (2017).
- ⁴⁴ K.W. Kim, L. O’Brien, P.A. Crowell, C. Leighton, and M.D. Stiles, *Phys. Rev. B* **95**, 1 (2017).
- ⁴⁵ K. Hamaya, T. Kurokawa, S. Oki, S. Yamada, T. Kanashima, and T. Taniyama, *Phys. Rev. B* **94**, 140401 (2016).

- ⁴⁶ L. O'Brien, M.J. Erickson, D. Spivak, H. Ambaye, R.J. Goyette, V. Lauter, P.A. Crowell, and C. Leighton, *Nat. Commun.* **5**, 3927 (2014).
- ⁴⁷ J.A. Mydosh, *Spin Glasses: An Experimental Introduction* (Taylor & Francis, London, 1993).
- ⁴⁸ G. Gruner and A. Zawadowski, *Reports Prog. Phys.* **37**, 1497 (1974).
- ⁴⁹ J. Kondo, S. Koikegami, K. Odagiri, K. Yamaji, and T. Yanagisawa, *The Physics of Dilute Magnetic Alloys* (Cambridge University Press, Cambridge, 2012).
- ⁵⁰ S.P. Dash, S. Sharma, J.C. Le Breton, J. Peiro, H. Jaffrès, J.-M. George, A.L. Lemaître, and R. Jansen, *Phys. Rev. B* **84**, 54410 (2011).
- ⁵¹ K.M. McCreary, A.G. Swartz, W. Han, J. Fabian, and R.K. Kawakami, *Phys. Rev. Lett.* **109**, 186604 (2012).
- ⁵² S. Vélez, V.N. Golovach, A. Bedoya-Pinto, M. Isasa, E. Sagasta, M. Abadia, C. Rogero, L.E. Hueso, F.S. Bergeret, and F. Casanova, *Phys. Rev. Lett.* **116**, 016603 (2016).
- ⁵³ R.K. Bennet, A. Hojem, and B.L. Zink, *Phys. Rev. B* **100**, 104404 (2019).
- ⁵⁴ See Supplemental Material at [URL] for further discussion on δR_{NL} and R_b in other material pairings and the isotropy of δR_{NL} with field direction.
- ⁵⁵ See Supplemental Material at [URL] for further discussion on Brillouin fits and Langevin fits to $\delta R_{NL}/R_{spin}$.
- ⁵⁶ S. Takahashi and S. Maekawa, *Phys. C Supercond. Its Appl.* **437–438**, 309 (2006).
- ⁵⁷ J. Bass and W.P. Pratt, *J. Phys. Condens. Matter* **19**, (2007).
- ⁵⁸ F. Beuneu and P. Monod, *Phys. Rev. B* **18**, 2422 (1978).
- ⁵⁹ K. Inoue and Y. Nakamura, *Phys. Status Solidi* **58**, 355 (1973).

- ⁶⁰ D. Goldhaber-Gordon, J. Göres, M.A. Kastner, H. Shtrikman, D. Mahalu, and U. Meirav, *Phys. Rev. Lett.* **81**, 5225 (1998).
- ⁶¹ W. Wei and G. Bergmann, *Phys. Rev. B* **37**, 5990 (1988).
- ⁶² P. Monod, *Phys. Rev. Lett.* **19**, 1113 (1967).
- ⁶³ E.W. Fenton, *Phys. Rev. B* **7**, 3144 (1973).
- ⁶⁴ V.I. Litvinov, *Phys. Status Solidi* **77**, 71 (1976).
- ⁶⁵ A.A. Abrikosov, *Phys. Phys. Fiz.* **2**, 61 (1965).
- ⁶⁶ H. Rohrer, *Phys. Rev.* **174**, 583 (1968).
- ⁶⁷ See Supplemental Material at [URL] for further discussion on fitting the spin relaxation rate with an alternative Kondo model.
- ⁶⁸ J. Kondo, *Prog. Theor. Phys.* **32**, 37 (1964).
- ⁶⁹ J.A. Appelbaum, *Phys. Rev.* **154**, 633 (1967).
- ⁷⁰ E.L. Wolf and D.L. Losee, *Phys. Rev. B* **2**, 3660 (1970).
- ⁷¹ J. Fabian, A. Matos-Abiague, C. Ertler, P. Stano, and I. Zutic, *Acta Phys. Slovaca* **57**, 565 (2007).
- ⁷² Y.J. Uemura, T. Yamazaki, D.R. Harshman, M. Senba, and E.J. Ansaldo, *Phys. Rev. B* **31**, 546 (1985).
- ⁷³ M.B. Salamon, *Phys. Rev.* **155**, 224 (1967).
- ⁷⁴ Y. Niimi, M. Kimata, Y. Omori, B. Gu, T. Ziman, S. Maekawa, A. Fert, and Y. Otani, *Phys. Rev. Lett.* **115**, 196602 (2015).
- ⁷⁵ T. Uchiyama, M. Matsui, and K. Adachi, *IEEE Trans. Magn.* **23**, 2305 (1987).
- ⁷⁶ D. Korn and G. Zibold, *J. Phys. F Met. Phys.* **15**, 2497 (1985).

⁷⁷ M.-K. Hou, M.B. Salamon, and T.A.L. Ziman, Phys. Rev. B **30**, 5239 (1984).

Figures

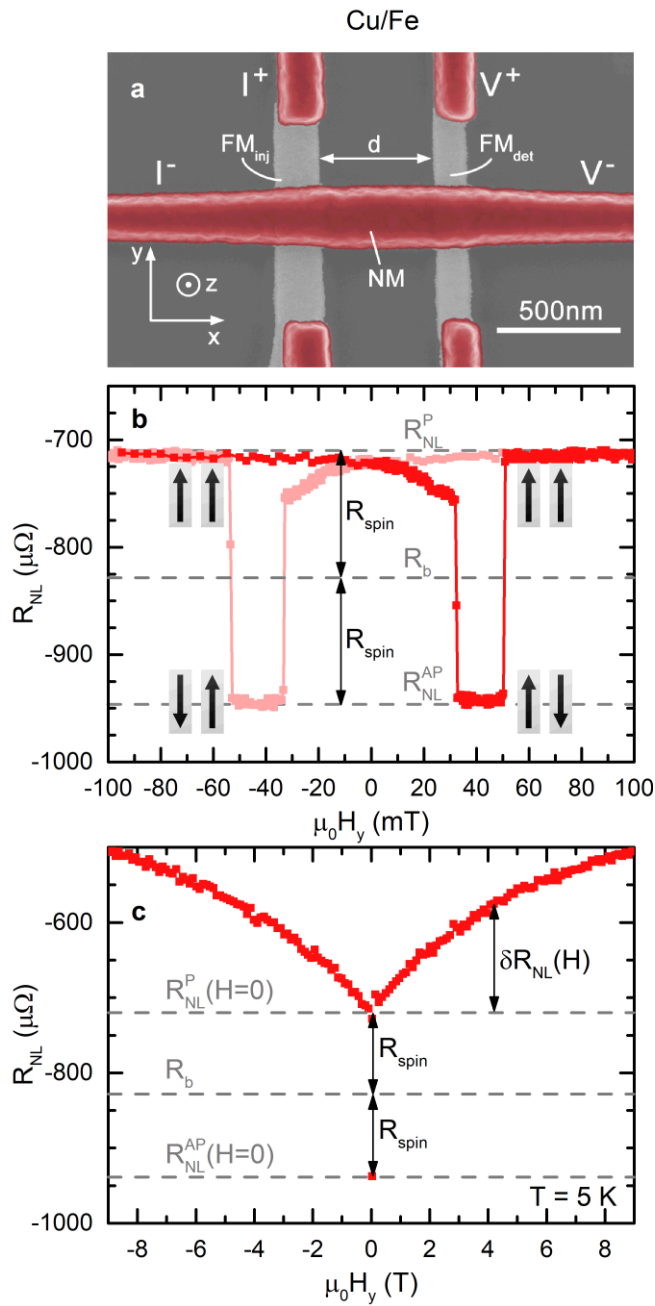


Figure 1 (a) False color SEM image of a Cu/Fe NLSV, with the non-magnetic metal (NM) and ferromagnetic (FM) materials highlighted. In the non-local geometry, a current (I) is injected at FM_{inj} and extracted from the far-left side of the NM channel, resulting in a non-equilibrium spin accumulation, manifest as a voltage (V_{NL}), measured between the far right of the NM channel and FM_{det} . (b) In-plane magnetic field (H_y) dependence of the non-local resistance, $R_{NL} = V_{NL}/I$, for a Cu/Fe NLSV with $d = 750$ nm, for forward (red) and reverse (pink) sweeps. The magnetization direction of the FM contacts are indicated by the arrows. $R_b = (R_{NL}^P + R_{NL}^{AP})/2$ is indicated on the figure. (c) Same as (b) up to larger (9 T) magnetic fields. Red solid squares show the measured data for parallel alignment of the FM contacts. The anti-parallel response at zero field is also shown, and the definitions of R_{spin} and δR_{NL}

are indicated. R_{NL}^P increases with field strength, beginning to saturate at sufficiently high fields, indicating a suppression of spin-flip scattering.

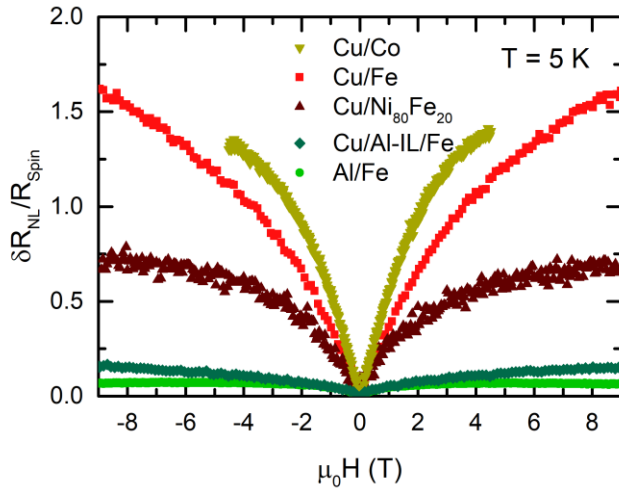


Figure 2 (Normalized) $\delta R_{NL}/R_{spin}$ as a function of in-plane applied magnetic field, for various materials. Devices shown have $d = 500$ nm except for Cu/Co and Cu/Ni₈₀Fe₂₀ which have $d = 400$ nm. Measurements of Cu/Co were taken only up to an applied field of $\mu_0 H = \pm 4.5$ T. The effect of in-plane applied magnetic field is most prominent for Cu/Co and Cu/Fe. For Cu/Al IL/Fe and Al/Fe, the effect is almost negligible.

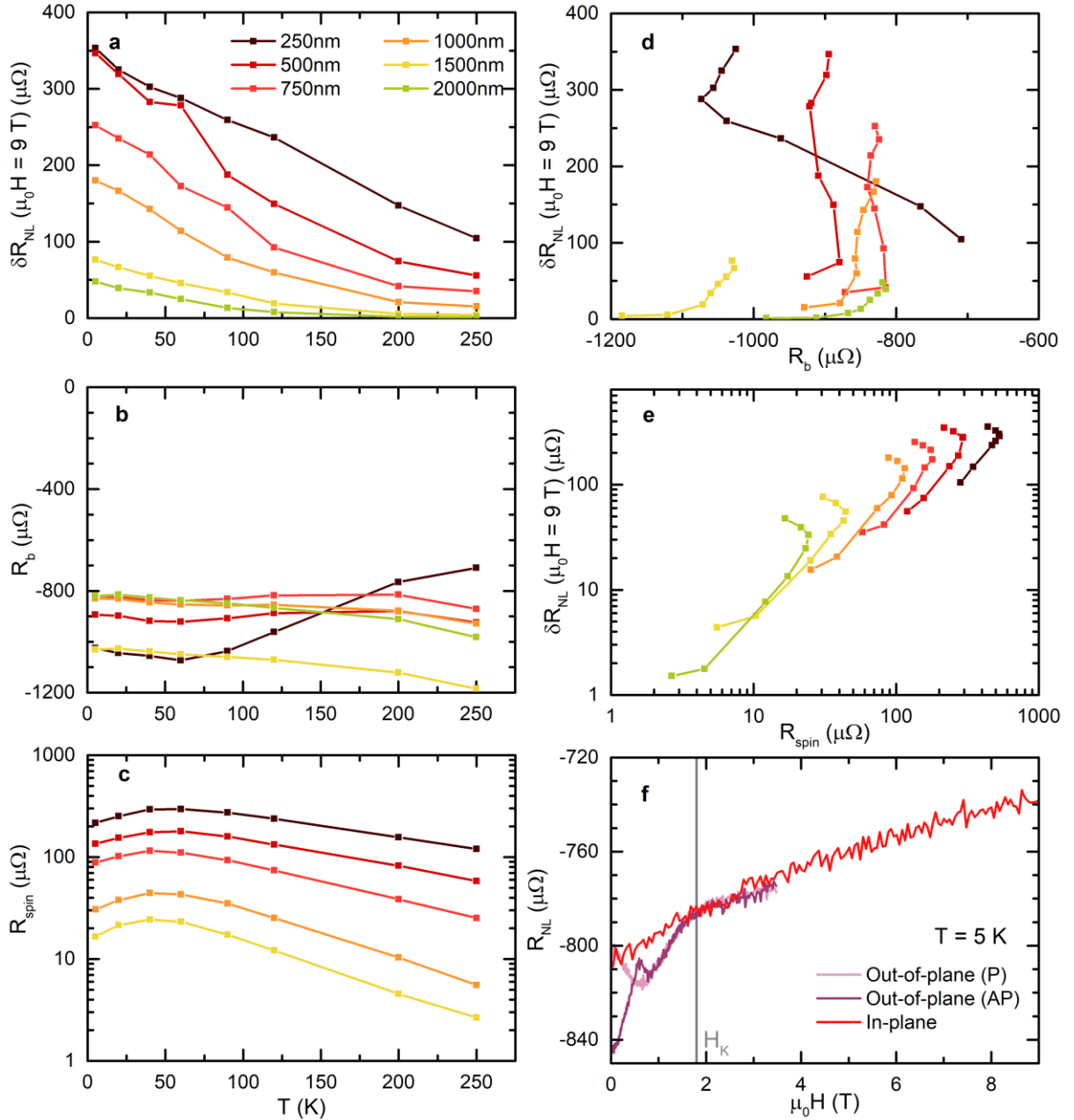


Figure 3 Temperature evolution of **(a)** $\delta R_{NL}(\mu_0 H = 9 T)$, **(b)** R_b and **(c)** R_{spin} for Cu/Fe NLSVs of various d . **(d)** Direct comparison of $\delta R_{NL}(\mu_0 H = 9 T)$ and R_b , demonstrating no correlation between the two parameters, and hence ruling out background effects as the origin of δR_{NL} . **(e)** $\delta R_{NL}(\mu_0 H = 9 T)$ as a function of R_{spin} . A clear, consistent correlation exists between the two, highlighting that δR_{NL} arises from spin-transport-related effects. **(f)** Field enhancement of R_{NL} for in-plane and out-of-plane (Hanle) measurements for a $d = 2000$ nm Cu/Fe NLSV at 5 K. Beyond the saturation field (H_K) of the FM contacts (vertical grey line) the in-plane and out-of-plane field responses of R_{NL} are identical, indicating that δR_{NL} is independent of applied field direction.

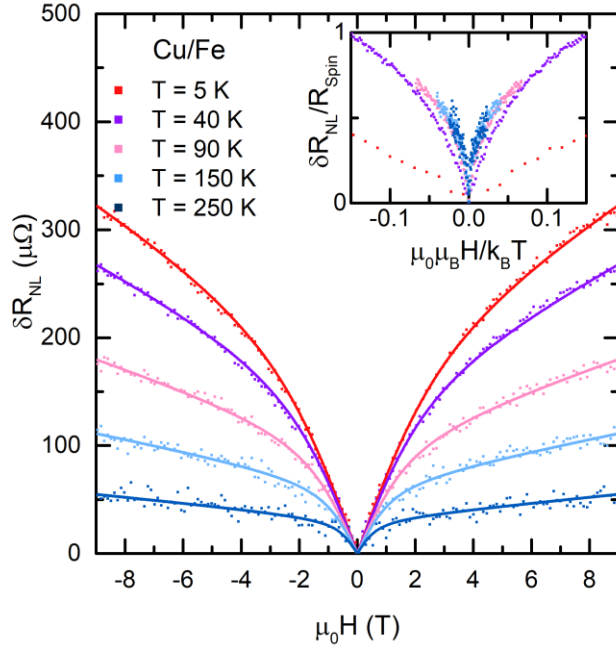


Figure 4 δR_{NL} as a function of $\mu_0 H$ for a Cu/Fe NLSV with $d = 500$ nm, at various temperatures. Solid lines are fits using equation (3), in order to model the data as a continuous function of field. Inset shows δR_{NL} normalized to R_{spin} as a function of $\mu_0 \mu_B H / k_B T$ for the same device. The 5 K data extends beyond the range of the plot. The data clearly do not collapse onto a single form, indicating that the field enhancement is not simply due to alignment of magnetic impurities.

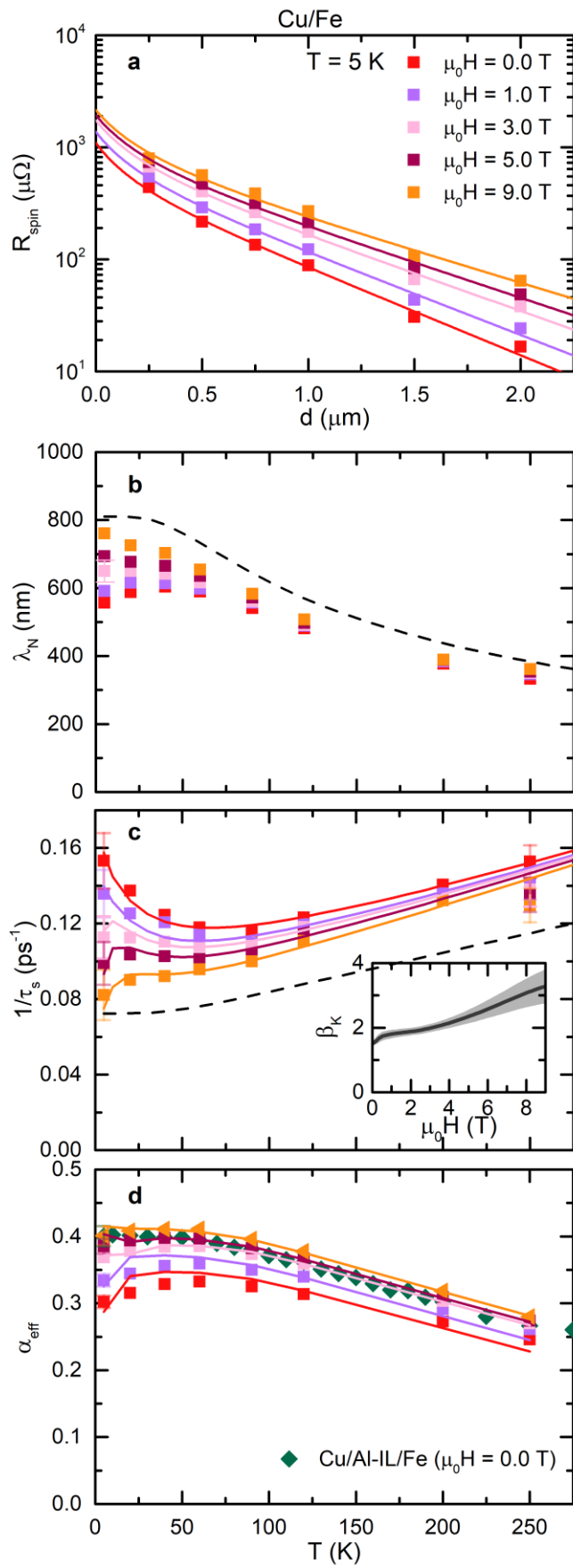


Figure 5 Data from measurements of Cu/Fe devices. For clarity, only select field strengths are shown, although a continuous range was available to us. **(a)** Variation of $R_{spin}(H)$ with d . Error bars are smaller than the symbol size. Solid lines are fits to the data using equation (4). **(b)** Spin diffusion length (λ_N) in the NM channel as a function of temperature. The dashed line is an estimate of the spin diffusion length from phonon and impurity scattering only. Error bars are smaller than the symbol size. **(c)** Same as (b) but for spin-flip scattering rate ($1/\tau_s$). Solid lines are fits using equations (1) and (6). For clarity, error bars are only shown for the first data points and last data points. (Inset) Quasi-continuous variation of β_K with field strength from fitting of data in (c). The light grey shaded area represents the uncertainty in the fit values. **(d)** Effective spin polarization, α_{eff} as a function of temperature. The zero-field and high-field (9 T) data are shown for a Cu/Fe device. Data from a Cu/Al-IL/Fe device at zero-field are also shown for comparison. Both devices have $d = 500$ nm. Under a high-field, α_{eff} for the Cu/Fe closely follows that of the Cu/Al-IL/Fe device, indicating that “normal” behavior has been restored.

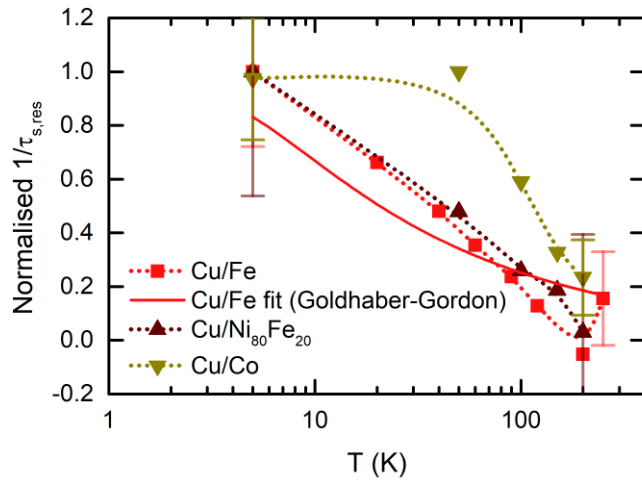


Figure 6 Normalized residual spin relaxation rate ($1/\tau_{s,res} = 1/\tau_s^{low\ field} - 1/\tau_s^{high\ field}$) as a function of temperature (\log_{10} scale), for Cu/Co, Cu/Fe and Cu/Ni₈₀Fe₂₀. The Cu/Fe data are fit using the phenomenological Goldhaber-Gordon expression of equation (5) (solid, red line). The Cu/Co and Cu/Ni₈₀Fe₂₀ data sets are incomplete and so should be treated only qualitatively. For these data, a guide to the eye (dotted line) is given. For clarity, error bars for only the first and last data points are shown.

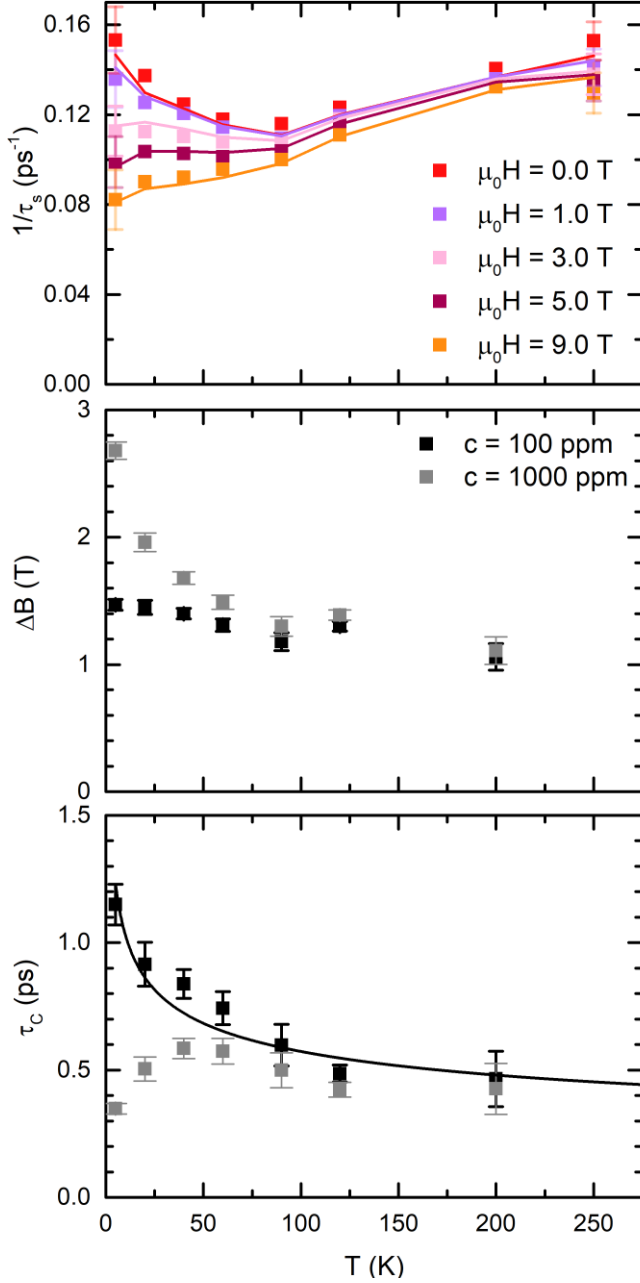


Figure 7 (a) The $1/\tau_s$ data (squares) for Cu/Fe NLSVs fit using equation (8) (solid lines), in order to test the applicability of the exchange model. The data are the same as in Fig. 5(c). A reasonable agreement between the data and the fit is achieved. Parameters **(b)** ΔB and **(c)** τ_c extracted from the fitting in (a) for $c = 100$ ppm and 1000 ppm, shown as a function of temperature. For $c = 100$ ppm, ΔB is independent of temperature, whereas τ_c increases with decreasing temperature, possibly indicating a spin glass transition. Fitting using a conventional description for spin glass dynamics (equation (10); solid line) reveals an unreasonably slow transition rate, however, indicating that a spin glass transition does not suitably describe the system. $c = 1000$ ppm yields an unreasonably large ΔB and non-trivial T dependence of τ_c . Anomalous 250 K data in ΔB and τ_c (likely arising from the large spread in $1/\tau_s$) have been removed.